Nano Energy 26 (2016) 466–478

Contents lists available at ScienceDirect

Nano Energy

journal homepage: www.elsevier.com/locate/nanoen

Design and synthesis of multiroom-structured metal compounds–carbon hybrid microspheres as anode materials for rechargeable batteries

Jung Sang Cho [a], Jong Min Won [a], Jung-Kul Lee [b,*], Yun Chan Kang [a,*]

[a] Department of Materials Science and Engineering, Korea University, Anam-Dong, Seongbuk-Gu, Seoul 136-713, Republic of Korea
[b] Department of Chemical Engineering, Konkuk University, 1 Hwayang-dong, Gwangjin-gu, Seoul 143-701, Republic of Korea

ARTICLE INFO

Article history:
Received 12 February 2016
Received in revised form
17 May 2016
Accepted 7 June 2016
Available online 7 June 2016

Keywords:
Nanostructure
Metal selenide
Lithium ion battery
Sodium ion battery
Spray pyrolysis

ABSTRACT

A novel structure denoted as a "multiroom carbon hybrid", which comprises empty voids dispersed in metal oxide-, sulfide-, and selenide-carbon composites is introduced. Multiroom-structured carbon hybrid microspheres of single component Co_3O_4 and NiO and multicomponent $(Ni_{0.5}Co_{0.5})O_x$ were successfully prepared using a one-pot spray pyrolysis process. Liquid-liquid phase segregation during the spray pyrolysis process is a key requirement for generating multiroom-structured metal oxide-carbon hybrid microspheres. Multiroom-structured $CoSe_2$-graphitic carbon (GC) and CoS_2-CoS-GC hybrid microspheres were also prepared using a simple post-treatment process. Multiroom-structured $CoSe_2$-GC hybrid microspheres have superior sodium-ion storage properties to bare $CoSe_2$ microspheres. The reversible discharge capacities of the $CoSe_2$-GC and CoS_2-CoS-GC hybrid microspheres for the 100th cycles at a current density of 0.2 A g^{-1} are 393 and 334 mA h g^{-1}, respectively. The discharge capacity of the multiroom-structured Co_3O_4-C hybrid microspheres for lithium-ion storage at a high current density of 3 A g^{-1} for the 150th cycle is 1243 mA h g^{-1}.

1. Introduction

Porous microspheres ranging in size from several micrometers to several tens of micrometers have many applications including rechargeable secondary batteries, solar cells, drug delivery agents, enzyme immobilization, gas sensors, and hydrogen evolution reactions [1–5]. The external and internal pore structures of the microspheres are critical to their application in various fields. Metal oxide microspheres with external and internal pores ranging in size from several nanometers to several tens of nanometers have mainly been studied for various liquid phase processes because of their mild preparation conditions and the slow formation of the nanostructure [6–9]. Self-assembling surfactant and block copolymers have been applied to form ordered pores within the metal oxide microspheres [10–12]. Organic and inorganic templates that are removable by simple washing or combustion processes have been applied to form interconnected voids within the metal oxide microspheres [13–15].

Spray pyrolysis, in which one droplet transforms into one microsphere via a gas-phase reaction, is advantageous for the one-pot preparation of porous microspheres with channeled pores or empty voids. Surfactant materials have been successfully applied to the preparation of mesoporous metal oxide microspheres. Lu et al. prepared mesostructured silica microspheres by applying CTAB as the surfactant template [16]. Silica/polymer nanocomposite microspheres showing reticulated foam structures were also prepared through the use of a PEO-PPO-PEO triblock copolymer (P123). Skrabalak et al. prepared macroporous carbon microspheres by spray pyrolysis using alkali-metal chloroacetate (CA) and dichloroacetate (DCA) [17]. However, reports on the synthesis of porous metal chalcogenide (i.e., metal sulfide and selenide) microspheres with controlled external and internal pore structures using either liquid-solution or spray-pyrolysis processes are scarce. Metal chalcogenide materials have attracted considerable attention owing to their excellent properties and wide applications in various fields including energy storage [18–21]. In addition, carbon materials have been applied as a suitable matrix to the anode materials for maintaining the structural integrity via accommodating the huge volume variations induced by Na^+ diffusion. Moreover, their high electroconductivity allows it derivatively serve as fast and continuous transport pathway for electrons upon cycling. These are responsible for improved electrochemical

* Corresponding authors.
E-mail addresses: jkrhee@konkuk.ac.kr (J.-K. Lee), yckang@korea.ac.kr (Y.C. Kang).

http://dx.doi.org/10.1016/j.nanoen.2016.06.012
2211-2855/

performance in Li and Na ion batteries [22–24].

In this study, unique structured carbon composite microspheres of transition metal oxide, sulfide, and selenide materials, which are denoted as "multiroom carbon hybrid" structures, were prepared through spray pyrolysis. Multiroom-structured transition metal oxide–carbon hybrid microspheres containing empty voids of several tens of nanometers were prepared by one-pot spray pyrolysis without applying surfactant and removable template materials. Multiroom-structured transition metal sulfide– and selenide–carbon hybrid microspheres were prepared by simple post-treatment of the spray pyrolysis product. In this study, carbon hybrid microspheres of single component Co_3O_4 and NiO and multicomponent $(Ni_{0.5}Co_{0.5})O_x$ were selected as the first target materials. The detailed formation mechanisms of the multiroom-structured Co_3O_4-carbon, CoS_2-carbon, and $CoSe_2$-carbon hybrid microspheres, which were focused on as representative examples, were investigated. In addition, the electrochemical properties of the multiroom-structured carbon hybrid microspheres of metal oxide and metal chalcogenides containing several tens of empty voids for lithium- and sodium-ion storage were investigated.

2. Experimental section

2.1. Sample preparation

Multiroom-structured transition metal oxide–carbon hybrid microspheres were prepared by one-pot spray pyrolysis. A schematic diagram of the spray pyrolysis system applied in this study is shown in Fig. S14. A large number of droplets were generated using a 1.7 MHz ultrasonic spray generator consisting of six vibrators. The droplets were carried to a quartz reactor (length = 1200 mm, diameter = 50 mm) by N_2 carrier gas at a flow rate of 25 L min^{-1}. For the multiroom-structured cobalt oxide–carbon hybrid microspheres, the spray solution was prepared by dissolving cobalt nitrate hexahydrate [$Co(NO_3)_2 \cdot 6H_2O$, 98%, Junsei] and dextrin [$(C_6H_{10}O_5)_n$, Samchun] in distilled water. The concentration of cobalt nitrate hexahydrate was fixed at 0.1 M. The appropriate amounts of dextrin were dissolved into the spray solution to generate concentrations of 5, 10, and 20 g L^{-1}. For the multiroom-structured carbon hybrid microspheres of NiO and multicomponent $(Ni_{0.5}Co_{0.5})O_x$, nickel nitrate hexahydrate [$(Ni(NO_3)_2) \cdot 6H_2O$, 98%, Sigma Aldrich] was used as the Ni source material. The multiroom-structured CoS_2-carbon and $CoSe_2$-carbon hybrid microspheres were prepared by sulfidation and selenization of the cobalt oxide–carbon hybrid microspheres, respectively. Selenium powders were used as the H_2Se gas source for selenization of the microspheres. The microspheres prepared by spray pyrolysis were loaded with the selenium powder into an alumina boat with a cover and placed in a quartz tube reactor, which was heated to 250 °C for 12 h under a flow of 10% H_2/Ar mixed gas. Thiourea powders were used as the H_2S gas source for sulfidation of the microspheres. The microspheres prepared by spray pyrolysis were loaded with the thiourea powder into an alumina boat with a cover and placed in a quartz tube reactor, which was heated to 180 °C for 6 h under a flow of 10% H_2/Ar mixed gas.

2.2. Characterization techniques

The microstructures of the microspheres were observed using field emission scanning electron microscopy (SEM; Hitachi, S-4800) and field emission transmission electron microscopy (TEM; JEOL, JEM-2100F). In addition, their crystal structures were evaluated with X-ray diffraction (XRD; X'Pert PRO MPD) using Cu K_α radiation (λ = 1.5418 Å) at the Korea Basic Science Institute (Daegu). X-Ray photoelectron spectroscopy (XPS; Thermo Scientific K-Alpha) with focused monochromatic Al K_α radiation at 12 kV and 20 mA was used to determine the compositions of the specimens. The surface areas of the powders were determined using the Brunauer–Emmett–Teller (BET) method with N_2 as the adsorbate gas. The structure of the carbon in the microspheres was characterized via Raman spectroscopy (Jobin Yvon LabRam HR800, excitation source: 632.8 nm He-Ne laser) at room temperature. Thermogravimetric analysis (TGA) was performed with a Pyris 1 TGA (Perkin Elmer, temperature range = 25–650 °C, heating rate = 10 °C min^{-1}, static air atmosphere).

2.3. Electrochemical measurements

The electrochemical properties of the microspheres were analyzed by constructing 2032-type coin cells. The anode was prepared by mixing the active material, carbon black, and sodium carboxymethyl cellulose (CMC) at a weight ratio of 7:2:1. Na metal for the sodium-ion batteries (NIBs) and Li metal for the lithium-ion batteries (LIBs) were used as the counter-electrodes, and microporous polypropylene film was used as the separator. The electrolyte was produced by dissolving 1 M $LiPF_6$ (Aldrich) into a mixture of fluoroethylene carbonate and dimethyl carbonate (FEC/DMC, 1:1 v/v) for the LIBs and 1 M $NaClO_4$ (Aldrich) into a mixture of ethylene carbonate/dimethyl carbonate (EC/DMC; 1:1 v/v) to which 5 wt% FEC was added for the NIBs. The discharge/charge characteristics of the samples were investigated by cycling over a potential range of 0.001–3 V at various current densities. Cyclic voltammograms were measured at a scan rate of 0.1 mV s^{-1}. The negative electrode containing the powders was 1 cm × 1 cm with a mass loading of approximately 1.2 mg cm^{-2}. In this study, the capacities of the samples were calculated based on the total mass of $CoSe_2$-C composite. In addition, the electrochemical impedance over a frequency range of 0.01 Hz–100 kHz was measured via electrochemical impedance spectroscopy (EIS).

3. Results and discussion

The mechanism of the formation of the multiroom-structured transition metal oxide–carbon hybrid microspheres containing several tens empty voids that were prepared by one-pot spray pyrolysis without applying surfactant and removable template materials is described in Fig. 1(a). The droplet containing the metal salts and dextrin, which was used as the carbon source material, was formed by an ultrasonic nebulizer (Fig. 1a-①). Drying of the droplet resulted in the formation of the metal salt–dextrin composite microsphere, and subsequent melting of the two components formed the composite microsphere with a dense structure (Fig. 1a-②). Liquid-liquid phase segregation within the melted powder resulted in the formation of the composite microspheres with inhomogeneous compositions. Phase segregation due to incongruent melting generated dextrin nanospheres several tens of nanometers large, which were confined within the metal salt nanorooms (Fig. 1a-③). Combustion and carbonization of the phase-segregated dextrin and decomposition of the metal salt under an N_2 atmosphere via the evolution of a large amount of gases generated the multiroom-structured metal oxide–carbon hybrid microspheres with several tens of empty voids (Fig. 1a-④). In this study, liquid-liquid phase segregation is a key requirement for the generation of multiroom-structured metal oxide–carbon hybrid microspheres. Therefore, the selection of metal salts and carbon source materials with appropriate melting temperatures before their decomposition will expand the strategy developed in this study for multiroom-structured metal oxide–carbon hybrid microspheres. One-step post-treatment of the product from spray pyrolysis under H_2S and H_2Se gas produced the multiroom-

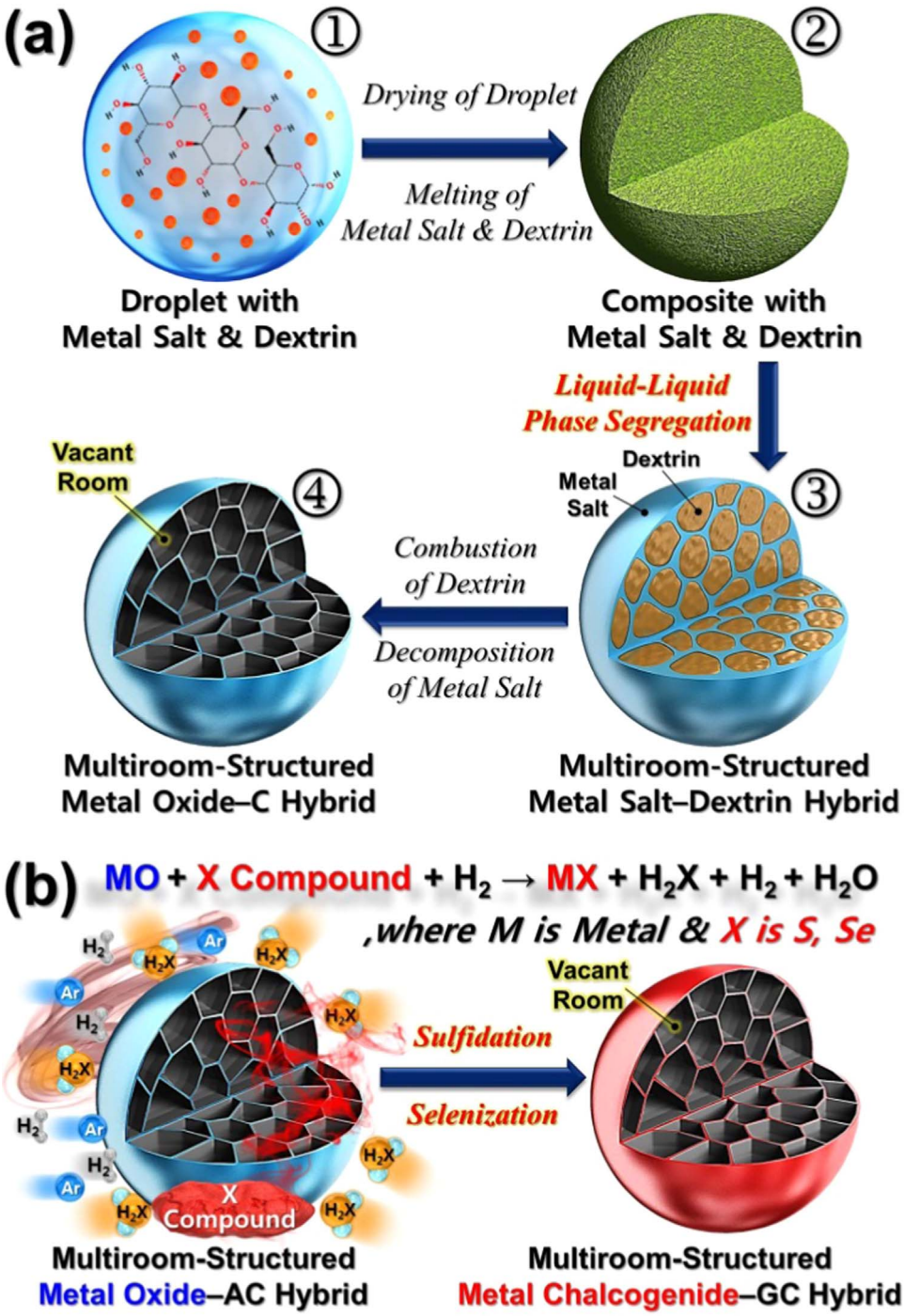

Fig. 1. Formation mechanism of (a) multiroom-structured transition metal oxide-carbon hybrid microspheres by one-pot spray pyrolysis and (b) multiroom-structured metal sulfide- and metal selenide-graphitic carbon hybrid microspheres by subsequent one-step post-treatment.

structured metal sulfide– and metal selenide–graphitic carbon hybrid microspheres with several tens of empty voids, respectively by the following reaction: Metal oxide + X Compound + H_2 → Metal chalcogenide + H_2X + H_2 + H_2O, where X is either S or Se element (Fig. 1(b)). The detail formation mechanism of nanorooms in the multiroom-structured transition metal chalcogenide-graphitic carbon (GC) composite microspheres by two-step process is described in Fig. S1.

The formation mechanism of the multiroom-structured hybrid microspheres via one-pot spray pyrolysis was elucidated on the basis of the morphology changes of the microspheres depending on their preparation conditions. The morphologies of the precursor microspheres prepared from the spray solutions containing different amounts of dextrin are shown in Fig. S2. The microspheres prepared by one-pot spray pyrolysis at 400 °C from the spray solution with an optimal amount of dextrin (10 g L^{-1}) shown in Fig. S2c have multiroom structures irrespective of the size of the microspheres. However, the microspheres prepared from the spray solutions with smaller amounts of dextrin (5 g L^{-1}) and larger amounts of dextrin (20 g L^{-1}) have hollow and dense structures, respectively, as shown in Figs. S2b and S2d, respectively. The bare cobalt oxide powders prepared from the spray solution without dextrin also have hollow structures, as shown in Fig. S2a. The microspheres were increasingly filled with increasing

concentration of dextrin in the spray solution. Melting of a large amount of dextrin resulted in microspheres with dense structures. After rinsing with distilled water, the microspheres prepared from the spray solution with large amounts of dextrin (20 g L^{-1}) also featured multiroom structures, as shown in Fig. S3. The color of the microspheres changed from dark brown to black upon rinsing. Therefore, it is evident that rinsing the dextrin nanospheres formed by liquid-liquid phase segregation generated empty nanovoids within the microspheres. The morphologies of the microspheres prepared at a relatively low temperature (300 °C) from the spray solution with the optimal amount of dextrin (10 g L^{-1}) are also shown in Fig. S4a. The incomplete decomposition of dextrin at 300 °C resulted in filled microspheres. However, rinsing the dextrin nanospheres formed by the liquid-liquid phase segregation process generated empty nanovoids within the microspheres, as shown in the SEM and TEM images in Figs. S4b–d. The high-resolution TEM image shown in Fig. S4e reveals ultrafine nanocrystals (< 5 nm). The inset image shown in Fig. S4e reveals clear lattice fringes separated by 0.29 nm, which corresponds to the (220) crystal plane of the cubic Co_3O_4 phase. Accordingly, cobalt nitrate decomposed even at 300 °C to form the Co_3O_4 backbone of the multiroom-structured microspheres. However, the presence of the ultrafine nanocrystals (< 5 nm) caused the SAED pattern to suggest an amorphous-like structure, as shown in Fig. S4f. From the results shown in Figs. S2–S4, the formation of dextrin nanospheres by liquid-liquid phase segregation played a key role in the production of multiroom-structured Co_3O_4-C hybrid microspheres.

The detailed morphologies of the multiroom-structured cobalt oxide–carbon hybrid microspheres, prepared by one-pot spray pyrolysis at 400 °C from the spray solution with the optimal amount of dextrin (10 g L^{-1}), are shown in Fig. 2. The SEM and low-resolution TEM images reveal uniform multiroom-structured cobalt oxide–carbon hybrids irrespective of the size of the microspheres. The SEM image of the crushed microsphere shown in the inset of Fig. 2(a) reveals empty multirooms divided by thin walls. As measured from the TEM images, the walls are less than 13 nm thick. The high-resolution TEM image shown in Fig. 2(f) reveals ultrafine nanodots uniformly dispersed within the thin walls. However, the SAED and XRD patterns shown in Fig. 2(g) and (h) suggest that the composite microspheres have amorphous-like structures because of the presence of the ultrafine nanocrystals.

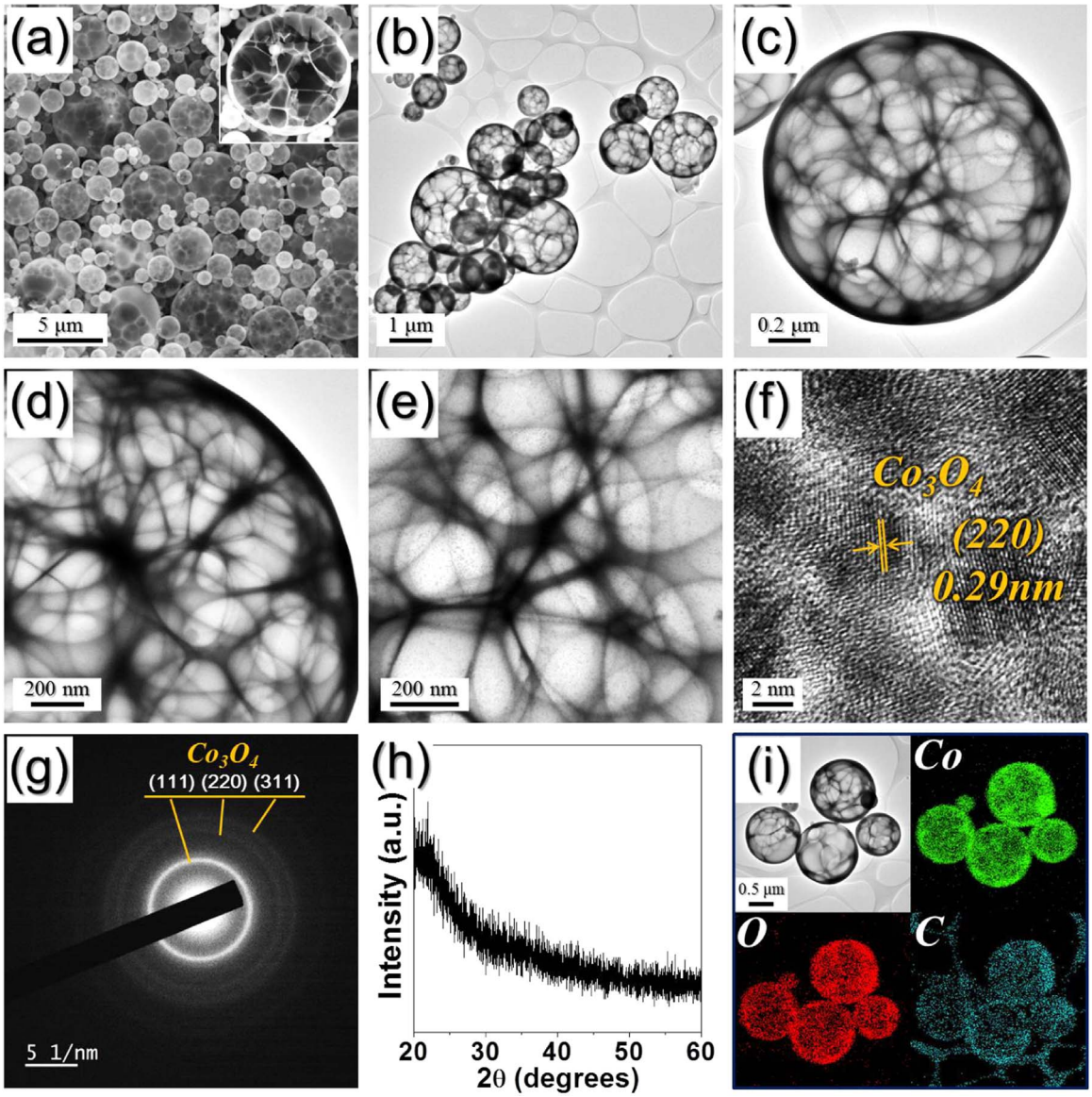

Fig. 2. Morphologies, SAED, XRD pattern, and elemental mapping images of the multiroom-structured cobalt oxide-C hybrid microspheres prepared from the spray solution with optimum amount of dextrin as 10 g L^{-1}: (a) SEM image, (b–e) TEM images, (f) HR-TEM image, (g) SAED pattern, (h) XRD pattern, and (i) elemental mapping images.

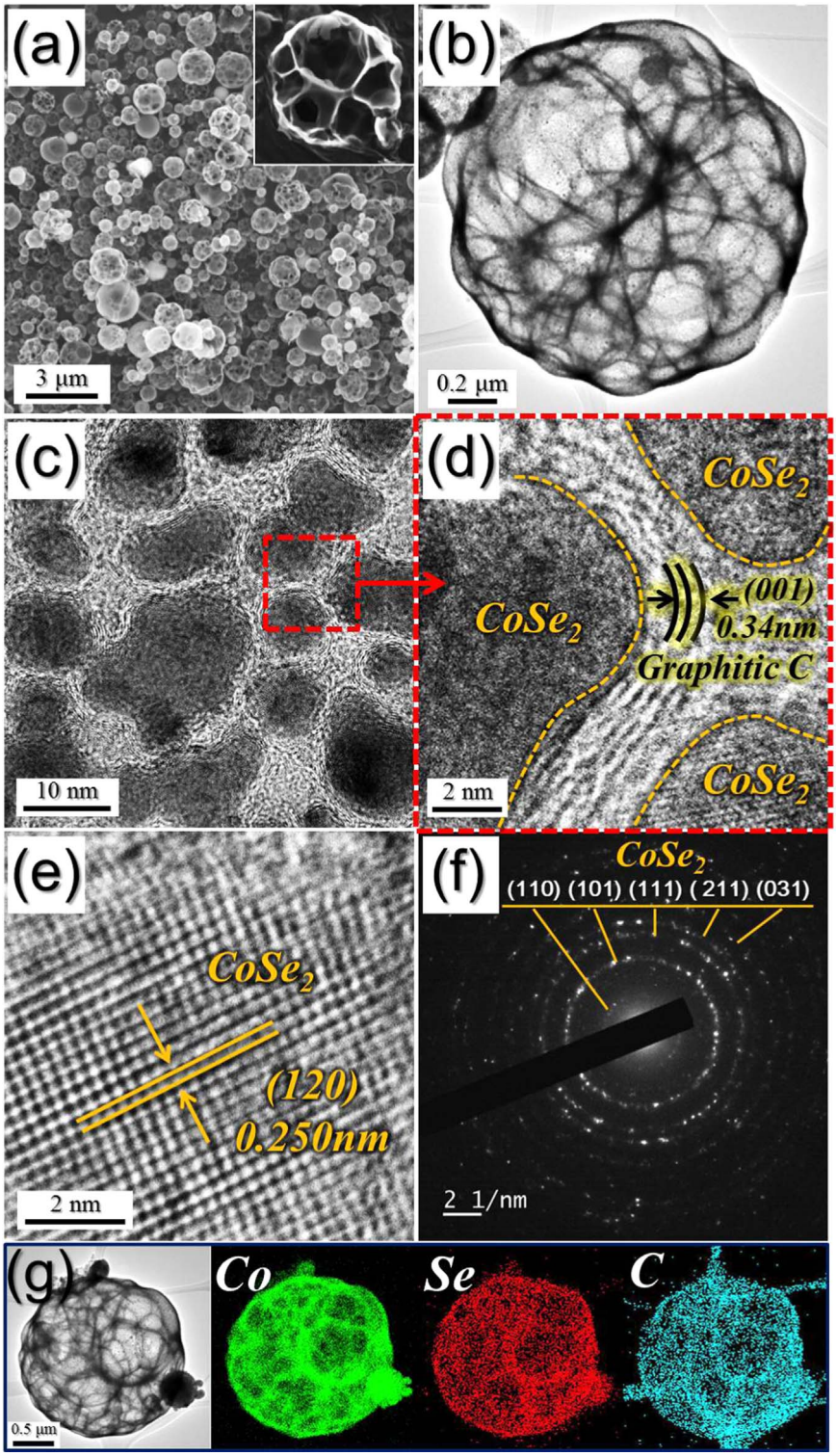

Fig. 3. Morphologies, SAED pattern, and elemental mapping images of the multiroom-structured cobalt selenide-graphitic carbon (GC) hybrid microspheres formed by selenization process: (a) SEM image, (b,c) TEM images, (d,e) HR-TEM images, (f) SAED pattern, and (g) elemental mapping images.

The elemental mapping images shown in Fig. 2(i) reveal uniform distribution of the Co and C components throughout the multi-room-structured cobalt oxide–carbon hybrid microspheres. The crystal growth of cobalt oxide did not occur at the preparation temperature of 400 °C because of the short residence time of 3.8 s. Therefore, the ultrafine cobalt oxide nanocrystals were uniformly distributed within the thin carbon walls formed by carbonization of dextrin.

The morphologies of the cobalt selenide–graphitic carbon (GC) hybrid microspheres formed by selenization of the multiroom-structured precursor microspheres are shown in Fig. 3. The process of selenization of the cobalt oxide-carbon hybrid microspheres is described in detail in Fig. 1(b). The XRD pattern shown in Fig. S5 reveals the formation of the $CoSe_2$-GC hybrid microspheres upon complete selenization of the microspheres. The hybrid microspheres feature pure orthorhombic $CoSe_2$ without any impurity

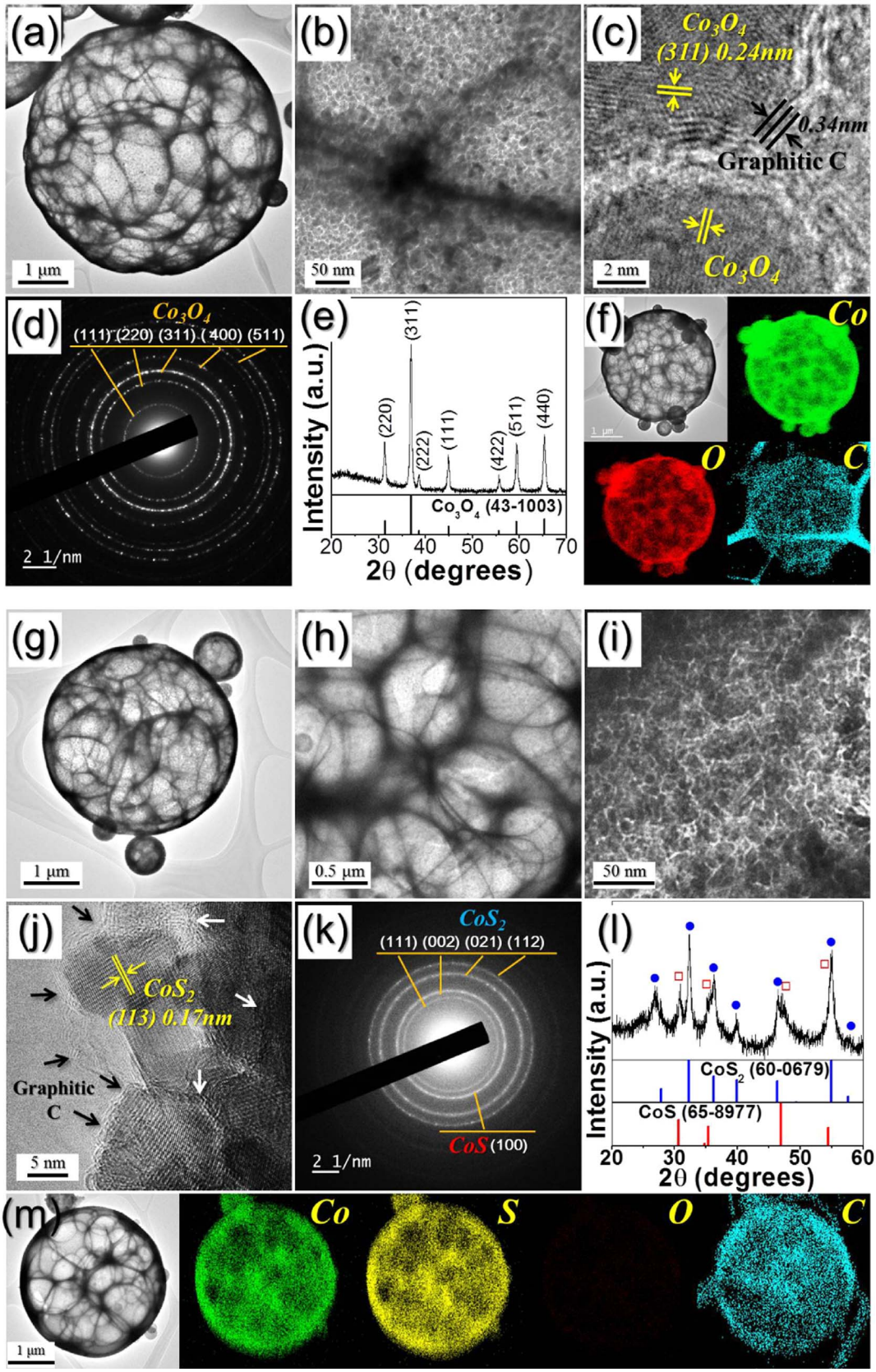

Fig. 4. Morphologies, SAED, XRD pattern, and elemental mapping images of the multiroom-structured (a–f) cobalt oxide-C composite microspheres formed by oxidation process and (g–m) cobalt sulfide-GC composite microspheres formed by sulfidation process: (a,b,g,h,i) TEM images, (c,j) HR-TEM images, (d,k) SAED patterns, (e,l) XRD patterns, and (f,m) elemental mapping images.

phases. The multirooms in the microspheres were well-maintained even after complete selenization, as evident from the SEM and low-resolution TEM images in Fig. 3(a) and (b). The TEM images shown in Fig. 3(c) and (d) reveal the ultrafine $CoSe_2$ nanocrystals and absence of necking between the nanocrystals. The mean size of the ultrafine $CoSe_2$ nanocrystals measured from the TEM images is 6.2 nm. During the selenization, metallic cobalt acted as a catalyst for the graphitization of amorphous carbon (AC) in the multiroom-structured spheres. With the help of metal catalyst, the activation energy of phase transformation from AC to GC could be lowered and thus the GC could be obtained under relatively low temperature [25–27]. Moreover, crystal growth of the $CoSe_2$ nanocrystals could be minimized because the GC formed by graphitization tightly encloses the $CoSe_2$ nanocrystals. GC layers with a lattice spacing of 0.34 nm are well-distributed between the $CoSe_2$ nanocrystals, as shown in Fig. 3(d). The high-resolution TEM image shown in Fig. 3(e) reveals clear lattice fringes separated by 0.25 nm, which corresponds to the (120) crystal plane of orthorhombic $CoSe_2$. The SAED pattern shown in Fig. 3(f) also reveals the formation of $CoSe_2$-GC hybrid microspheres without impurity phases. The elemental mapping images shown in Fig. 3(g) confirm the uniform distribution of ultrafine $CoSe_2$ nanocrystals throughout the multiroom-structured GC microspheres. The chemical states and molecular environments of the multiroom-structured $CoSe_2$-GC hybrid microspheres were characterized via XPS. In the Co 2p spectrum of the multiroom-structured $CoSe_2$-GC hybrid microspheres, as shown in Fig. S6a, the main peaks occur at binding energies of 778.2 eV for Co $2p_{3/2}$ and 793.1 eV for Co $2p_{1/2}$; these are characteristic of $CoSe_2$ [28–30]. In the Se 3d spectrum shown in Fig. S6b, the binding energies at 54.55 eV for Se $3d_{5/2}$ and 55.31 eV for Se $3d_{3/2}$ were also confirmed to be in good agreement with the reported values for $CoSe_2$ in the literature [28–30]. Additionally, a peak was observed at 58.2 eV correspond to Se–O bond which is attributed to the SeO_2 impurity due to the exposure of the sample under an air. It shows that a small amount of Se was deposited inside the porous structure of $CoSe_2$-GC hybrid microspheres during the selenization process. The C 1*s* spectrum shown in Fig. S6c reveals peaks corresponding to sp^2-bonded carbon (C–C assigned to graphitic carbon) and carboxylic (C=O) components at 284.6 and 288.2 eV, respectively [31–33]. The peak corresponding to the C–C bond exhibits high intensity, whereas that associated with the C=O bond has low intensity. This indicates that the graphitic carbon was formed by graphitization mechanism during the selenization process. The Raman spectrum shown in Fig. S7a contains the characteristic wide *D* and *G* bands of carbon around 1340 and 1590 cm^{-1}, respectively. The *G* band $\sim$1590 cm^{-1} corresponds to the first order scattering of E2g modes, i.e. bond stretching of all pairs of sp^2 atoms in both rings and chains. The *D*-band is related to the defects in the graphitic carbon such as bond-angle disorder, bond-length disorder, vacancies, edge defects, etc. Therefore, the lower of the ratio of I_D/I_G, the better of the crystallization of carbon materials. The ratio of I_D/I_G in the sample is about 1.9. indicating the formation of graphitic carbon in the multiroom-structured $CoSe_2$-GC hybrid. The TGA curve of the multiroom-structured $CoSe_2$-GC hybrid microspheres shown in Fig. S7b suggests that a several-step weight loss process occurs at temperatures below 600 °C. The steep weight losses observed at temperatures around 430 and 520 °C were attributed to combustion of GC and decomposition of $CoSe_2$ into Co_3O_4, respectively. A GC content of 16% was estimated from the TGA results of the multiroom-structured $CoSe_2$-GC hybrid microspheres.

The morphologies of the multiroom-structured cobalt oxide– and cobalt sulfide–carbon hybrid microspheres formed by oxidation and sulfidation of the multiroom-structured precursor microspheres are shown in Fig. 4. The multiroom-structured cobalt oxide–carbon hybrid microspheres were obtained by oxidation of the multiroom-structured precursor microspheres at 400 °C for 1 h under ambient atmosphere. Sulfidation of the multiroom-structured precursor microspheres at 180 °C for 6 h under H_2S gas produced the cobalt sulfide–carbon hybrid microspheres. The XRD patterns shown in Fig. 4(e) and (l) support the formation of the Co_3O_4-C and CoS_2-CoS-C hybrid microspheres by complete oxidation and sulfidation, respectively. The multiroom structure of the precursor microspheres was well-maintained in the Co_3O_4-C and CoS_2-CoS-C hybrid microspheres, as evident from the SEM and TEM images in Fig. 4. Ultrafine Co_3O_4 and cobalt sulfide nanocrystals are well-distributed throughout the thin walls in the Co_3O_4-C and CoS_2-CoS-C hybrid microspheres, as shown in Fig. 4 (b) and (i), respectively. The high-resolution TEM images shown in Fig. 4(c) and (j) feature lattice fringes separated by 0.24 and 0.17 nm, respectively, which correspond to the (311) and (113) crystal planes of Co_3O_4 and CoS_2 phases, respectively. The SAED patterns shown in Fig. 4(d) and (k) also support the formation of Co_3O_4-C and CoS_2-CoS-C hybrid microspheres, respectively. The elemental mapping images shown in Fig. 4(f) and (m) confirm the uniform distribution of ultrafine Co_3O_4 and cobalt sulfide nanocrystals throughout the multiroom-structured carbon microspheres, respectively.

For comparison, bare $CoSe_2$ microspheres were also prepared by selenization of the bare Co_3O_4 microspheres by post-treatment of the multiroom-structured precursor microspheres at 500 °C for 1 h under ambient atmosphere. The morphologies and XRD patterns of the microspheres obtained before and after selenization are shown in Fig. S8. The XRD patterns of the microspheres reveal the presence of cubic Co_3O_4 and cubic $CoSe_2$ microspheres before and after selenization, respectively; in addition, some of the multiroom-structured precursor microspheres transformed into hollow-structured Co_3O_4 microspheres. The multiroom structure was destroyed because of the decomposition of carbon material during post-treatment under ambient atmosphere. The bare $CoSe_2$ microspheres have similar morphologies to those of the bare Co_3O_4 microspheres. The BET surface areas of the bare $CoSe_2$ and multiroom-structured $CoSe_2$-GC hybrid microspheres are 24 and 17 $m^2\ g^{-1}$, respectively (Fig. S9).

Furthermore, the strategy described in this study was generally applied to various multiroom-structured metal oxide–carbon hybrid microspheres. We successfully synthesized multiroom-structured single and multicomponent metal oxide–carbon hybrid microspheres using one-pot spray pyrolysis. The morphologies and XRD patterns of the multiroom-structured NiO-C hybrid and NiO microspheres before and after post-treatment at 400 °C under ambient atmosphere are shown in Fig. S10. The multiroom-structured NiO-C hybrid microspheres prepared by one-pot spray pyrolysis have ultrafine NiO nanocrystals uniformly dispersed within the carbon microspheres, as evident from the high-resolution TEM image in Fig. S10c. The SAED and XRD patterns shown in Figs. S10d and S10e, respectively, also support the formation of ultrafine NiO nanocrystals in carbon matrix. The carbon-free NiO microspheres obtained after post-treatment at 400 °C for 1 h under ambient atmosphere also have multiroom structures, as shown in Figs. S10g and S10k. The NiO nanocrystals grew during the post-treatment process. The mean size of the NiO nanocrystals comprising the multiroom structure, as measured from the high-resolution TEM image shown in Fig. S10i, is 17 nm. The SAED and XRD patterns and elemental mapping images shown in Figs. S109j–l confirm the formation of carbon-free multiroom-structured NiO microspheres. The characteristics of the multiroom-structured multicomponent oxide-carbon hybrid microspheres with the same molar contents of the Ni and Co components prepared by one-pot spray pyrolysis are shown in Fig. 5. The Ni, Co, and C components are well-distributed throughout the multiroom-structured hybrid microspheres with amorphous-like

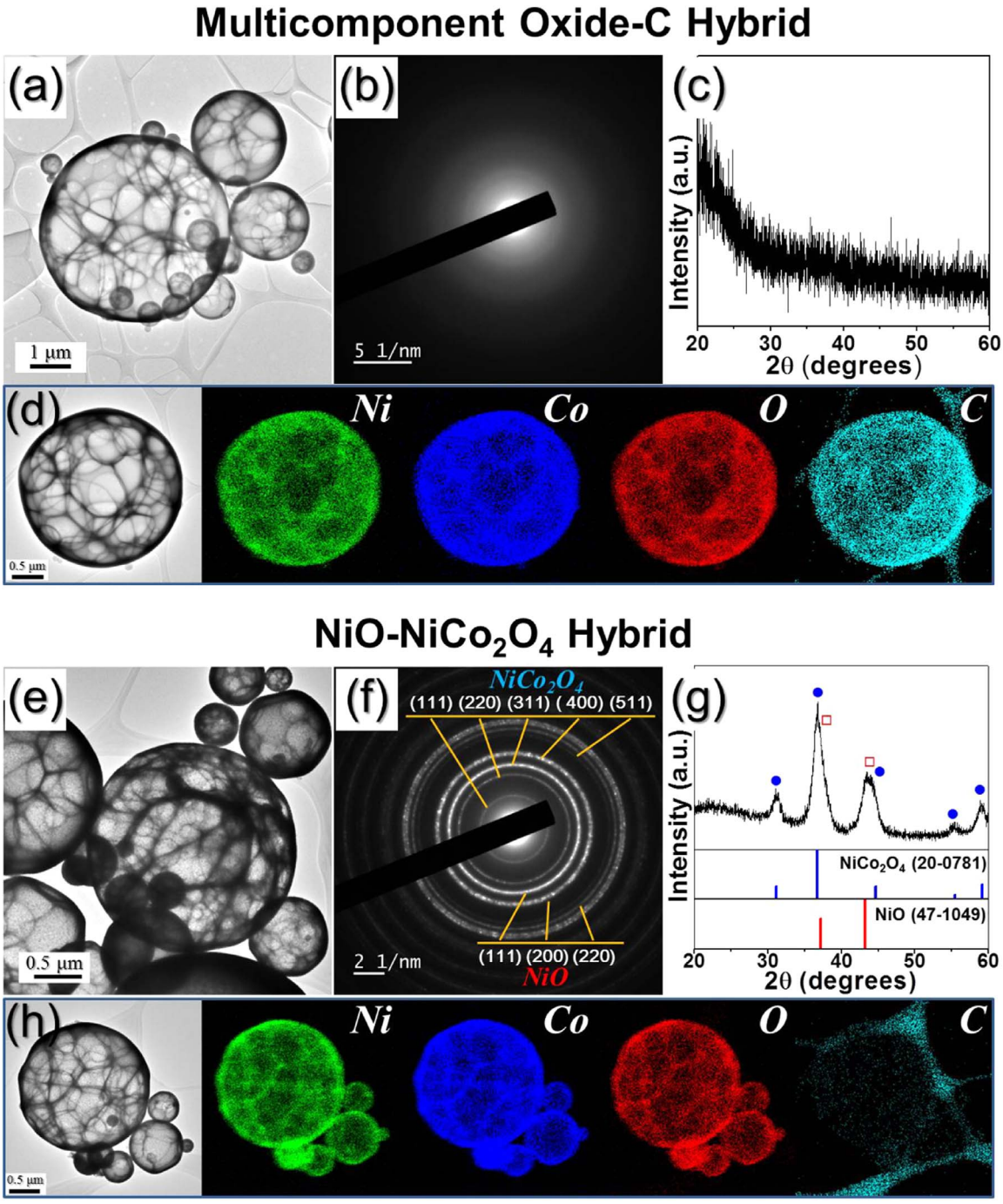

Fig. 5. Morphologies, SAED, XRD pattern, and elemental mapping images of the (a–d) as-prepared multiroom-structured multicomponent oxide-carbon hybrid microspheres with the same molar contents of the Ni and Co components prepared by one-pot spray pyrolysis and (e–h) multiroom-structured carbon-free multicomponent metal oxide microspheres obtained after post-treatment at 400 °C for 1 h under ambient atmosphere: (a,e) TEM images, (b,f) SAED patterns, (c,g) XRD patterns, and (d,h) elemental mapping images.

structures, as shown in Fig. 5b–d. The carbon-free multicomponent metal oxide microspheres obtained after post-treatment at 400 °C for 1 h under ambient atmosphere also feature multiroom structures, as shown in Fig. 5(e). The SAED and XRD patterns shown in Fig. 5(f) and (g) reveal the formation of multiroom-structured microspheres with mixed crystal structures of $NiCo_2O_4$ and NiO phases. However, the Ni and Co components are well-distributed throughout these multiroom-structured microspheres, as shown in Fig. 5(h).

The electrochemical properties of the multiroom-structured $CoSe_2$-GC hybrid microspheres for use in Na-ion storage were compared to those of the bare $CoSe_2$ microspheres (Fig. 6). The CV curves of the bare $CoSe_2$ and multiroom-structured $CoSe_2$-GC hybrid microspheres for the first five cycles at a scan rate of 0.1 mV s^{-1} in the voltage range of 0.001–3 V are shown in Fig. 6 (a) and (b), respectively. The CV curves of the bare $CoSe_2$ microspheres have a sharp reduction peak at around 0.75 V in the first cathodic scan; this was attributed to the following reaction: $CoSe_x + 2xNa^+ + 2xe^- \leftrightarrow Co + xNa_2Se$ [34,35]. In contrast, the CV curves of the multiroom-structured $CoSe_2$-GC hybrid microspheres have two broad reduction peaks at around 1.08 and 0.88 V in the first cathodic scan. The first reduction peak centered at 1.08 V

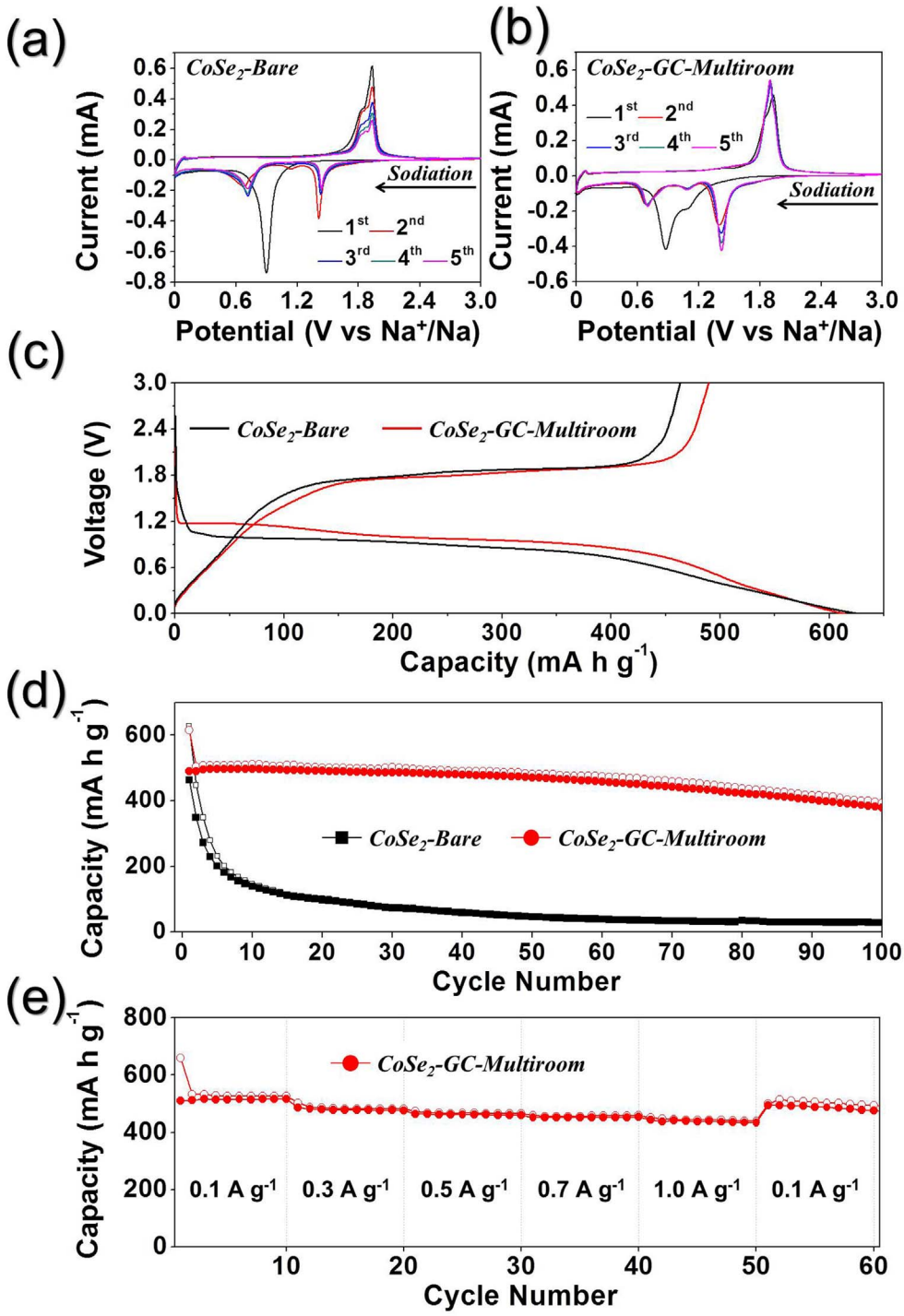

Fig. 6. Electrochemical properties of the multiroom-structured $CoSe_2$-GC hybrid microspheres and bare $CoSe_2$ hollow microspheres: CV curves of the (a) bare $CoSe_2$ hollow microspheres and (b) multiroom-structured $CoSe_2$-GC hybrid microspheres at a scan rate of 0.1 mV s^{-1}, (c) first charge-discharge curves at a current density of 0.2 A g^{-1}, (d) cycling performances at a current density of 0.2 A g^{-1}, and (e) rate performance of the multiroom-structured $CoSe_2$-GC hybrid microspheres.

could be attributed to the transformation of metalloid Se to Na_2Se [36]. The small amount of metalloid Se deposited inside the porous structure of $CoSe_2$-GC hybrid microspheres during selenization process as confirmed by XPS analysis. The intense peak located around 0.88 V is indicative of the above conversion reaction of $CoSe_x$ into metallic Co and the formation of Na_2Se [34,35]. The sharp oxidation peaks of the two samples observed at around 1.90 V in the first anodic scan were attributed to recovery of $CoSe_x$ material from the metallic Co nanocrystals and Na_2Se [34,35]. The reduction peaks of the two samples transformed into the broad reduction peaks at around 1.43 V after the first cycle because of the conversion of the $CoSe_x$ nanocrystals into ultrafine nanocrystals during the first cycle [37,38]. The new reduction peaks that appeared at around 1.14 and 0.69 V in subsequent cycles were ascribed to a multistep electrochemical reaction corresponding to sodiation. According to previous reports regarding CoS_2 and $FeSe_2$ anodes for NIBs [34,35], the discharge and charge process can be summarized by Eqs (1)–(4):

Discharge process:

$$CoSe_2 + xNa^+ + xe^- \rightarrow Na_xCoSe_2 \quad (1)$$

$$Na_xCoSe_2 + (2-x)Na^+ + (2-x)e^- \rightarrow CoSe + Na_2Se \quad (2)$$

$$CoSe + 2Na^+ + 2e^- \rightarrow Co + Na_2Se \quad (3)$$

Charge process:

$$Co + 2Na_2Se \rightarrow CoSe_2 + 4Na^+ + 4e^- \quad (4)$$

The initial discharge and charge curves for the two samples at a constant current density of 0.2 A g^{-1} are shown in Fig. 6(c). The discharge curve of the bare $CoSe_2$ microspheres features a clear long plateau at around 1.0 V; this corresponds to the sharp reduction peak in the CV curve shown in Fig. 6(a). On the other hand, the discharge curve of the $CoSe_2$-GC hybrid microspheres features two plateaus at around 1.18 and 1.0 V. The results of the initial discharge and charge curves are in good agreement with those of the CV curves. The initial discharge capacities of the $CoSe_2$-GC hybrid and bare $CoSe_2$ microspheres are 614 and 627 mA h g^{-1}, respectively, and their corresponding initial Coulombic efficiencies are 80% and 74%, respectively. Accordingly, it is apparent that the GC did not decrease the initial Coulombic efficiency of the $CoSe_2$-GC hybrid microspheres. The cycling performances of the two samples at a constant current density of 0.2 A g^{-1} are shown in Fig. 6(d). The discharge capacities of the $CoSe_2$-GC hybrid and bare $CoSe_2$ microspheres for the 100th cycle are 393 and 29 mA h g^{-1}, respectively, and their capacity retentions measured from the second cycle are 78% and 6%, respectively. The discharge capacities of the bare $CoSe_2$ microspheres dropped from 627 to 148 mA h g^{-1} during the first 10 cycles. In contrast, the discharge capacities of the $CoSe_2$-GC hybrid microspheres decreased slowly over 100 cycles. The rate performance of the $CoSe_2$-GC hybrid microspheres is shown in Fig. 6(e): The current density increased in a step-wise manner from 0.1 to 1.0 A g^{-1}. The reversible discharge capacities of the $CoSe_2$-GC hybrid microspheres slightly decreased from 526 to 451 mA h g^{-1} as the current densities increased from 0.1 to 1.0 A g^{-1}. In addition, the discharge capacities recovered well to 514 mA h g^{-1} when the current density was returned to 0.1 A g^{-1} after the rate performance tests.

EIS measurements before and after 1, 30, and 50 cycles were performed to reveal that the electrochemical properties of the multiroom-structured $CoSe_2$-GC hybrid microspheres are superior to those of the bare $CoSe_2$ microspheres with similar structures. The Nyquist plots shown in Fig. 7 were obtained by deconvolution with a Randle-type equivalent circuit model (Fig. S11) [39–41]. The equivalent circuit model describes the electrochemical reaction steps, including Na ion migration through the solid electrolyte interphase layers, the charge transfer reaction, and Na ion diffusion kinetics throughout the active materials [42,43] The medium frequency semicircle in the Nyquist plots was attributed to the charge-transfer resistance (R_{ct}) between the active material and the electrolyte; the low frequency region corresponds to the sodium diffusion process within the electrodes [44–46]. The $CoSe_2$-GC hybrid microspheres with high electrical conductivity have

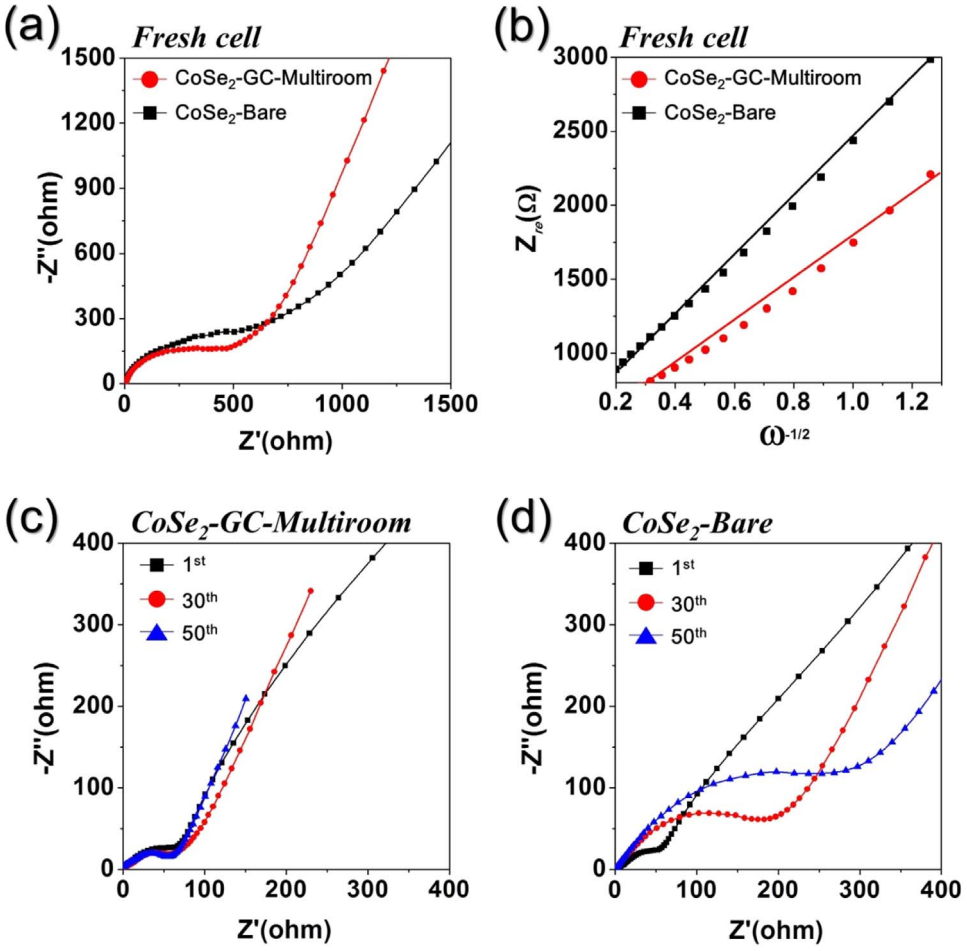

Fig. 7. Nyquist impedance plots and relationships between the real part of the impedance (Z_{re}) and $\omega^{-1/2}$ of multiroom-structured $CoSe_2$-GC hybrid microspheres: (a) Nyquist impedance plots before cycling, (b) relationships between the real part of the impedance (Z_{re}) and $\omega^{-1/2}$ before cycling, (c) Nyquist impedance plots after cycling of multiroom-structured $CoSe_2$-GC, and (d) Nyquist impedance plots after cycling of bare $CoSe_2$.

lower R_{ct} value of 492 Ω than that of 678 Ω for the bare $CoSe_2$ microspheres before cycling, as shown in Fig. 7(a). Fig. 7(b) shows the relationship between Z_{re} and $\omega^{-1/2}$ in the low frequency (f) region, where ω is the angular frequency ($\omega = 2\pi f$). The less steep slope at the low frequency indicated higher sodium ion diffusivity in the multiroom-structured $CoSe_2$-GC hybrid microspheres [47]. The structure composing $CoSe_2$ nanoparticles surrounded with GC provided high sodium ion diffusivity in the multiroom-structured $CoSe_2$-GC hybrid microspheres. The charge-transfer resistances of the two samples decreased after the first cycle because of the formation of ultrafine nanocrystals during the first discharge and charge processes [37,38]. The charge-transfer resistances of the $CoSe_2$-GC hybrid microspheres were 67, 69, and 70 Ω at 1, 30, and 50 cycles, respectively, in which the R_{ct} value almost did not increase during 50 cycles, as shown in Fig. 7(c). However, the charge-transfer resistances of the bare $CoSe_2$ microspheres increased with increasing number of cycles, as shown in Fig. 7(d). The R_{ct} values of the bare $CoSe_2$ microspheres at 1, 30, and 50 cycles shown in Fig. 7(d) were 68, 201, and 320 Ω, respectively. The multiroom-structured GC matrix dramatically improved the electrochemical properties of the $CoSe_2$ material for sodium-ion storage via this improved structural stability. The $CoSe_2$ nanocrystals embedded within the GC matrix were not pulverized during the repeated sodium-ion insertion and de-insertion processes. Moreover, GC matrix derivatively served as fast and continuous transport pathways for electrons upon cycling due to its high electrical conductivity. The morphologies of the multiroom-structured $CoSe_2$-GC hybrid microspheres and bare $CoSe_2$ hollow microspheres obtained after 100 cycles were investigated by SEM and TEM analysis. The multiroom-structured $CoSe_2$-GC hybrid microspheres maintained their morphologies quite well even after repeated sodium insertion and desertion processes as shown by SEM and TEM images in Fig. S12a. However, the bare $CoSe_2$ hollow microspheres were broken into several pieces and aggregated after 100 cycles as shown in Fig. S12b.

The electrochemical properties of the multiroom-structured CoS_2-CoS-C hybrid microspheres for sodium-ion storage are shown in Fig. 8. Fig. 8(a) shows the CV curves of the CoS_2-CoS-C microspheres during the first five cycles. Two broad reduction peaks were observed at 0.96 and 0.66 V during the first cathodic scan; these were assigned to the formation of Co metal and Na_2O, resulting from the conversion of the Na ions with CoS_2 and CoS [34,48,49]. The three reduction peaks at around 1.41, 0.88, and 0.49 V, which were ascribed to a multistep electrochemical reaction corresponding to sodiation, were observed after the first cycle. The broad oxidation peak observed at around 1.86 V during the first anodic scan was attributed to recovery of CoS_x material from the metallic Co nanocrystals and Na_2S [34,48,49]. The two

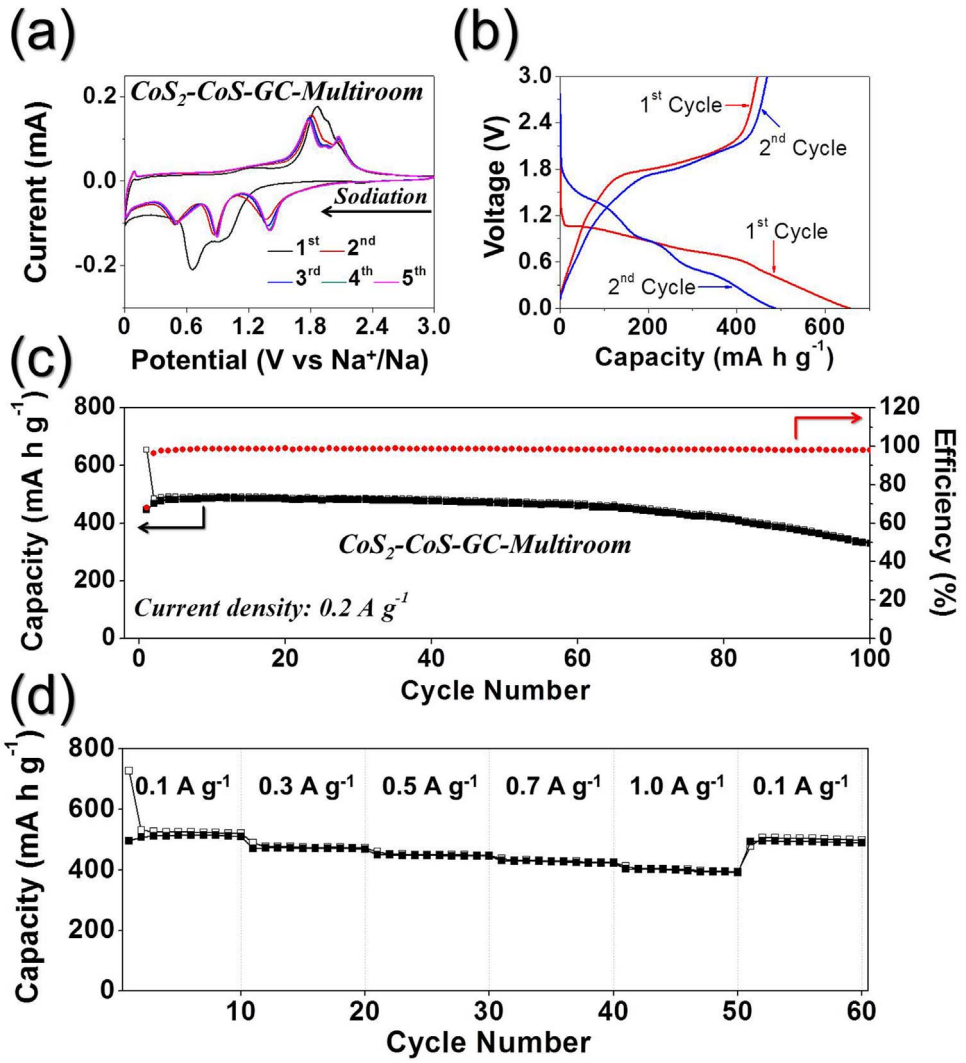

Fig. 8. Electrochemical properties of the multiroom-structured CoS_2-CoS-GC hybrid microspheres formed by sulfidation process: (a) CV curves at a scan rate of 0.1 mV s^{-1}, (b) first and second charge-discharge curves at a current density of 0.2 A g^{-1}, (c) cycling performance and corresponding Coulombic efficiencies at a current density of 0.2 A g^{-1}, and (d) rate performance.

oxidation peaks that are present after the first cycle represent the formation of intermediate Na_xCoSe_2 and fully charged $CoSe_2$ [34,48,49]. The initial discharge and charge capacities of the multiroom-structured CoS_2-CoS-C hybrid microspheres at a current density of 0.2 A g^{-1} shown in Fig. 8(b) are 655 and 446 mA h g^{-1}, respectively, and their corresponding initial Coulombic efficiency is 68%. The discharge capacities for the 2nd and 100th cycle are 487 and 334 mA h g^{-1}, respectively, and their capacity retention measured from the second cycle is 69%. The rate performance of the multiroom-structured CoS_2-CoS-C hybrid microspheres is shown in Fig. 8(c). The current density increased in a step-wise manner from 0.1 to 1.0 A g^{-1}. The reversible discharge capacities of the CoS_2-CoS-C hybrid microspheres slightly decreased from 530 to 411 mA h g^{-1} as the current densities increased from 0.1 to 1.0 A g^{-1}. In addition, the discharge capacities recovered well to 506 mA h g^{-1} when the current density was returned to 0.1 A g^{-1} after the rate performance test. The cobalt oxide materials have better electrochemical properties for Li-ion storage than for Na-ion storage. Therefore, the electrochemical properties of the multiroom-structured Co_3O_4-C hybrid microspheres for Li-ion storage are shown in Fig. S13. The CV and charge/discharge curves of the Co_3O_4-C microspheres are shown in Figs. S13a and S13b, respectively. The sharp reduction peak at around 0.88 V in the CV curve and long plateau region at around 0.97 V in the initial discharge curve correspond to Li^+ insertion into the crystal structure of Co_3O_4 and reduction of the Co ions to Co metal, respectively [50–52]. The discharge capacities of the multiroom-structured Co_3O_4-C hybrid microspheres at a high current density of 3 A g^{-1} for the 2nd and 150th cycle are 1007 and 1243 mA h g^{-1}, respectively. The rate performance of the multiroom-structured Co_3O_4-C hybrid microspheres is shown in Fig. S13c. The current density increased in a step-wise manner from 1 to 10 A g^{-1}. The reversible discharge capacities of the Co_3O_4-C hybrid microspheres slightly decreased from 1024 to 858 mA h g^{-1} as the current densities increased from 1 to 10 A g^{-1}. In addition, the discharge capacities recovered well to 1078 mA h g^{-1} when the current density was returned to 1 A g^{-1} after the rate performance tests at high current densities.

4. Conclusions

In this study, unique structured carbon composite microspheres of transition metal oxide, sulfide, and selenide materials were prepared for the first time, and their electrochemical properties as anode materials for NIBs and LIBs were studied. Multiroom-structured transition metal oxide–carbon hybrid microspheres containing several tens of empty voids were prepared by one-pot spray pyrolysis; these were transformed into metal selenide– and metal sulfide–graphitic carbon hybrid microspheres via a one-step post-treatment process without undergoing morphological changes. The multiroom-structured graphitic carbon hybrid microspheres with high structural stability during cycling have excellent electrochemical properties for Li-ion and Na-ion storage. Liquid-liquid phase segregation due to incongruent melting of the metal salt and dextrin resulted in the multiroom-structured transition metal oxide–carbon hybrid microspheres containing several tens of empty voids. Therefore, the new strategy developed in this study could be applied for the preparation of multiroom-structured transition metal oxide–, selenide–, and sulfide–carbon hybrid microspheres with various compositions for a wide variety of applications including energy storage.

Acknowledgment

This work was supported by the National Research Foundation of Korea (NRF) grant funded by the Korea government (MEST) (No. 2012R1A2A2A02046367). This work was supported by the Energy Efficiency & Resources Core Technology Program of the Korea Institute of Energy Technology Evaluation and Planning (KETEP), granted financial resource from the Ministry of Trade, Industry & Energy, Republic of Korea (201320200000420 and 20153030091450).

Appendix A. Supporting information

Supplementary data associated with this article can be found in the online version at http://dx.doi.org/10.1016/j.nanoen.2016.06.012.

References

[1] M. Hartmann, X. Kostrov, Chem. Soc. Rev. 42 (2013) 6277–6289.
[2] A.D. Roberts, X. Li, H. Zhang, Chem. Soc. Rev. 43 (2014) 4341–4356.
[3] F. Rodríguez-Reinoso, A. Sepúlveda-Escribano, in: H.S. Nalwa (Ed.) Handbook of Surfaces and Interfaces of Materials, Academic Press Burlington, 2001, pp. 309–355.
[4] W. Yuan, Y. Tang, X. Yang, Z. Wan, Appl. Energy 94 (2012) 309–329.
[5] L. Ji, M. Gu, Y. Shao, X. Li, M.H. Engelhard, B.W. Arey, W. Wang, Z. Nie, J. Xiao, C. Wang, J.-G. Zhang, J. Liu, Adv. Mater. 26 (2014) 2901–2908.
[6] X. Fang, Z. Liu, M.-F. Hsieh, M. Chen, P. Liu, C. Chen, N. Zheng, ACS Nano 6 (2012) 4434–4444.
[7] D.G. Shchukin, R.A. Caruso, Chem. Mater. 16 (2004) 2287–2292.
[8] W. Zeng, C. Dong, B. Miao, H. Zhang, S. Xu, X. Ding, S. Hussain, Mater. Lett. 117 (2014) 41–44.
[9] Q. Xie, Y. Ma, X. Wang, D. Zeng, L. Wang, L. Mai, D.L. Peng, ACS Nano 10 (2016) 1283–1291.
[10] A.E. Garcia-Bennett, N. Kupferschmidt, Y. Sakamoto, S. Che, O. Terasaki, Angew. Chem. Int. Ed. 44 (2005) 5317–5322.
[11] S.A. Jenekhe, X.L. Chen, Science 283 (1999) 372–375.
[12] B. Xie, H. Shi, G. Liu, Y. Zhou, Y. Wang, Y. Zhao, D. Wang, Chem. Mater. 20 (2008) 3099–3104.
[13] A.H. Lu, F. Schüth, Adv. Mater. 18 (2006) 1793–1805.
[14] U. Meyer, A. Larsson, H.P. Hentze, R.A. Caruso, Adv. Mater. 14 (2002) 1768–1772.
[15] Y. Wan, Y. Shi, D. Zhao, Chem. Commun. 9 (2007) 897–926.
[16] Y. Lu, H. Fan, A. Stump, T.L. Ward, T. Rieker, C.J. Brinker, Nature 398 (1999) 223–226.
[17] S.E. Skrabalak, K.S. Suslick, J. Am. Chem. Soc. 128 (2006) 12642–12643.
[18] D. Aldakov, A. Lefrançois, P. Reiss, J. Mater. Chem. C 1 (2013) 3756–3776.
[19] A. Fernando, K.D.M. Weerawardene, N.V. Karimova, C.M. Aikens, Chem. Rev. 115 (2015) 6112–6216.
[20] X. Liu, J. Du, C. Li, X. Han, X. Hu, F. Cheng, J. Chen, J. Mater. Chem. A 3 (2015) 3425–3431.
[21] S.V. Kershaw, A.S. Susha, A.L. Rogach, Chem. Soc. Rev. 42 (2013) 3033–3087.
[22] H. Wang, H. Dai, Chem. Soc. Rev. 42 (2013) 3088–3113.
[23] Y. Shi, L. Peng, Y. Ding, Y. Zhao, G. Yu, Chem. Soc. Rev. 44 (2015) 6684–6696.
[24] P. Xiong, B. Liu, V. Teran, Y. Zhao, L. Peng, X. Wang, G. Yu, ACS Nano 8 (2014) 8610–8616.
[25] Y.-Z. Chen, H. Medina, H.-C. Lin, H.-W. Tsai, T.-Y. Su, Y.-L. Chueh, Nanoscale 7 (2015) 1678–1687.
[26] Y.J. Hong, J.S. Cho, Y.C. Kang, Chem. -Eur. J. 21 (2015) 18202–18208.
[27] M. Xie, J. Yang, J. Liang, X. Guo, W. Ding, Carbon 77 (2014) 215–225.
[28] M.-R. Gao, Y.-F. Xu, J. Jiang, Y.-R. Zheng, S.-H. Yu, J. Am. Chem. Soc. 134 (2012) 2930–2933.
[29] D. Kong, H. Wang, Z. Lu, Y. Cui, J. Am. Chem. Soc. 136 (2014) 4897–4900.
[30] Y.R. Zheng, M.R. Gao, Q. Gao, H.H. Li, J. Xu, Z.Y. Wu, S.H. Yu, Small 11 (2015) 182–188.
[31] M.-C. Lin, M. Gong, B. Lu, Y. Wu, D.-Y. Wang, M. Guan, M. Angell, C. Chen, J. Yang, B.-J. Hwang, Nature 520 (2015) 324–328.
[32] G.D. Park, J.S. Cho, Y.C. Kang, Nano Energy 17 (2015) 17–26.
[33] X. Zhang, Y. Jiao, L. Sun, L. Wang, A. Wu, H. Yan, M. Meng, C. Tian, B. Jiang, Nanoscale 8 (2015) 2418–2427.
[34] Z. Fu, Z. Shadike, M.-H. Cao, F. Ding, L. Sang, Chem. Commun. 51 (2015) 10486–10489.
[35] K. Zhang, Z. Hu, X. Liu, Z. Tao, J. Chen, Adv. Mater. 27 (2015) 3305–3309.
[36] C. Luo, Y. Xu, Y. Zhu, Y. Liu, S. Zheng, Y. Liu, A. Langrock, C. Wang, ACS Nano 7 (2013) 8003–8010.
[37] J.S. Cho, J.M. Won, J.-H. Lee, Y.C. Kang, Nanoscale 46 (2015) 19620–19626.
[38] Y. Sun, X. Hu, W. Luo, F. Xia, Y. Huang, Adv. Funct. Mater. 23 (2013) 2436–2444.

[39] J.S. Cho, Y.J. Hong, J.-H. Lee, Y.C. Kang, Nanoscale 7 (2015) 8361–8367.
[40] J.S. Cho, Y.C. Kang, Small 11 (2015) 4673–4681.
[41] D.T. Ngo, R.S. Kalubarme, H.T. Le, J.G. Fisher, C.N. Park, I.D. Kim, C.J. Park, Adv. Funct. Mater. 24 (2014) 5291–5298.
[42] H. Wu, M. Xu, Y. Wang, G. Zheng, Nano Res. 6 (2013) 167–173.
[43] H. Wu, M. Xu, H. Wu, J. Xu, Y. Wang, Z. Peng, G. Zheng, J. Mater. Chem. 22 (2012) 19821–19825.
[44] J.S. Cho, Y.J. Hong, Y.C. Kang, ACS Nano 9 (2015) 4026–4035.
[45] Z. Wang, D. Luan, S. Madhavi, Y. Hu, X.W.D. Lou, Energy Environ. Sci. 5 (2012) 5252–5256.
[46] Y. Xu, Y. Zhu, Y. Liu, C. Wang, Adv. Energy Mater. 3 (2013) 128–133.
[47] G.Q. Liu, H.T. Kuo, R.S. Liu, C.H. Shen, D.S. Shy, X.K. Xing, J.M. Chen, J. Alloy. Compd. 496 (2010) 512–516.
[48] Y. Du, X. Zhu, X. Zhou, L. Hu, Z. Dai, J. Bao, J. Mater. Chem. A 3 (2015) 6787–6791.
[49] Y.N. Ko, Y.C. Kang, Carbon 94 (2015) 85–90.
[50] G. Huang, F. Zhang, X. Du, Y. Qin, D. Yin, L. Wang, ACS Nano 9 (2015) 1592–1599.
[51] M. Reddy, G. Subba Rao, B. Chowdari, Chem. Rev. 113 (2013) 5364–5457.
[52] J. Wang, N. Yang, H. Tang, Z. Dong, Q. Jin, M. Yang, D. Kisailus, H. Zhao, Z. Tang, D. Wang, Angew. Chem. Int. Ed. 125 (2013) 6545–6548.

Jung Sang Cho is a postdoctoral research fellow at the Nano Electronic Materials Laboratory, Department of Materials Science and Engineering, Korea University, Korea under Prof. Yun Chan Kang's supervision. He received his Ph. D. from the Interdisciplinary Program for Bioengineering, College of Engineering, Seoul National University, Korea in 2013. His research interests focuses on the design, synthesis, and characterization of the nanostructured materials for the energy storage, sensor, display, and biomaterials by using spray pyrolysis, spray drying, and electrospinning processes

Jong Min Won received his B.S. degree from the Department of Chemical Engineering, Konkuk University, Korea in 2014. He is currently a Ph. D candidate in the Department of Materials Science and Engineering, Korea University, Korea. His research focuses on the development of nanostructured electrode materials for lithium and sodium ion batteries using spray pyrolysis and spray drying

Jung-Kul Lee received his Ph. D. from Biological Sciences, Korea Advanced Institute of Science and Technology (KAIST), South Korea in 1999, and had post-doc experience at the Biomolecular and Chemical Engineering, University of Illinois at Urbana-Champaign in USA (2004-2006). He is currently a Professor at the Department of Chemical Engineering, Konkuk University, South Korea since 2006. His research group works on protein engineering and nano-catalysts

Yan chan Kang received his Ph. D. from Chemical Engineering, Korea Advanced Institute of Science and Technology (KAIST), Korea in 1997, and had post-doc experience at the Chemical Engineering, Hiroshima University in Japan (1997-1998). He returned to Korea, and joined KRICT as a senior researcher (2000-2003). He became a Professor of the Department of Chemical Engineering, Konkuk University, Korea (2004-2014). He is currently a Professor of the Department of Materials Science and Engineering, Korea University, Korea since 2014. His research group works on the development of nanostructured materials for the energy storage by aerosol process. For details please see the lab website: http://spray.korea.ac.kr.